A wavenumber domain numerical analysis of rail noise including the surface impedance of the ground

Jungsoo Ryue*[a], Seungho Jang[b], David J. Thompson[c]

[a]*School of Naval Architecture and Ocean Engineering, University of Ulsan, Ulsan 44610, South Korea*
[b]*Korea Railroad Research Institute, Uiwang 16105, South Korea*
[c]*Institute of Sound and Vibration Research, University of Southampton, Southampton SO17 1BJ, UK*

*Corresponding author: jsryue@ulsan.ac.kr

Abstract

In most previous studies of sound radiation from railway rails, the rail has been regarded as located in free space, disregarding the influence of the ground. However, in order to predict the noise from the rail more precisely, the effect of the ground should be included in rolling noise predictions. In this study, the rail noise is investigated by means of a wavenumber domain numerical method, including the presence of the ground. For rails attached to a rigid ground or located at a certain distance above it, the influence of the ground is examined in terms of the radiation ratio and longitudinal directivity. From the prediction of radiated power, it is found that the vertical and lateral bending waves of the rail radiate most of the noise for the corresponding direction. Hence, a simplified calculation is proposed that only includes these waves, instead of a full three-dimensional analysis. An absorptive ground is also modelled by applying impedance boundary conditions at the ground surface to investigate the influence of the ground on the rail noise. Finally, for the vertical and lateral bending waves in the rail, the cross-sectional directivity of the noise is predicted for various surface impedances of the ground. It is found that the simplified calculation proposed in this study is valid for the prediction of noise from the rail. Also the presence of the ground and its impedance condition have considerable effects on the level and directivity patterns of the noise radiated from the rail.

1. Introduction

Rolling noise is known to be one of the main sources of environmental noise from railways, particularly for conventional train speeds. The rolling noise is produced by vibration of the track and wheel, which is induced by the roughness of their surfaces at the wheel/rail contact area. For ballasted tracks, the main sources of rolling noise are the sleepers, the rails and the wheels. These three components contribute in different frequency ranges of roughly up to 400 Hz, from 400 to 2000 Hz and above 2000 Hz, respectively, the exact ranges depending on the track and wheel types. Since, in terms of overall noise level, the rail is often the most significant among these three sources of rolling

noise, it is important to understand the characteristics of the noise radiated by the rail if the railway noise is to be reduced and quieter railway track systems are to be developed.

Analytical formulations for rolling noise were first presented by Remington [1, 2] over four decades ago. He determined the rail radiation by approximating it as a cylinder [3]. Later these rolling noise models were developed and extended by Thompson and a software package, known as Track-Wheel Interaction Noise Software (TWINS), was developed [4, 5]. Within TWINS, the sound radiation is evaluated by using radiation ratios obtained from a two-dimensional (2D) equivalent source model. Thompson et al. [6] have investigated the radiation ratio of the rail noise with simple 2D boundary element models (BEM) and have shown that the 2D model gives good agreement with the three-dimensional (3D) results for most frequencies.

The wavenumber domain analysis method is very useful for structures which have a uniform cross-section and infinite length in one direction. A rail is ideally suited to such a wavenumber domain analysis. The waveguide finite element method (WFE) and similar numerical wave-based approaches have previously been applied to the vibration analysis of rails [7–11]. This method is also referred to as wavenumber FE, 2.5 dimensional (2.5D) FE or the semi-analytical FE method in the literature [12, 13]. Nilsson et al. [7] have extended this wavenumber domain approach by combining the WFEs with waveguide boundary elements (WBEs) and used this combined method to investigate the sound radiation from an embedded rail as well as a rail in free space. This method allows a three-dimensional analysis of the sound radiation from an infinite rail. From the results it was shown that, in terms of the radiation ratio for vertical excitation, the results from a 2D radiation model coincide well with the full 3D calculation for frequencies above the first cut-on of vertical bending waves. Below this frequency, the rail radiates more like a point source and the 2D approximation is no longer valid. In their work, however, the ground was not included in the model.

In most previous studies on railway rolling noise, the sound power from the rail has been determined by regarding it as a noise source located in free space, disregarding the presence of the ground [6, 7]. Instead, the effect of the ground has been introduced in a simplified way, such as through a directivity index or a reflection coefficient within sound propagation models [14, 15], or by using numerical methods [16, 17]. However, in order to predict the noise radiated from the rail more precisely, the effect of the ground may need to be included in the sound power calculations. Zhang et al. [18] have investigated the effect of the ground on the radiation ratio of a rail by using a 2D boundary element method; they also introduced corrections into the model to consider the wavenumbers of the propagating waves in the rail. The influence of a partially absorptive ground, where the rail is either attached to the ground, or located at some distance above it, was predicted in terms of the radiation ratio and validated with experiments for an unsupported rail. In their predictions, however, the authors focused only on the radiation ratio due to a rigid body motion of the rail in either vertical or lateral directions. So they only used a 2D boundary element model without modelling the rail vibration, and thus disregarded the rail cross-section deformation.

The directivity of noise radiated by a rail has also been investigated by a few researchers. Kitagawa and Thompson [19, 20] have investigated the longitudinal directivity of rail noise and the effect on the sound measured with a microphone array. It was shown from their study that the rail radiates in a certain direction relative to the normal,

which is determined by the ratio of wavenumbers in the air and the rail. Zhang and Jonasson [21] have studied the cross-sectional directivity of rail noise experimentally on a test track. They measured the cross-sectional directivity in one-third octave bands for vertical excitation.

In the present study, the rail noise is investigated by means of the coupled waveguide finite and boundary element method, including the presence of the ground. Similar to ref. [18], three cases are considered: a rail in free space, a rail attached to the ground and a rail located at a certain distance above the ground. The effect of ground absorption is studied by introducing an impedance boundary on the surface of the ground and the influence on the radiation ratio and cross-sectional distribution of the rail noise is studied. In order to improve efficiency, a method is proposed based on a single wavenumber at each frequency. The WFE/BE method is briefly summarised in Sec. 2 and the various models are introduced in Sec. 3. Results are presented in Sec. 4 for a rail in free space, in Sec. 5 for a rail with a rigid ground and in Sec. 6 for a rail with an absorptive ground.

2. Wavenumber domain numerical method

In this section, the WFE/BE method used in this study is described briefly; for further details the reader may refer to refs [7, 22–25]. The same method has also been used to predict the vibro-acoustic behaviour of panels [26, 27]. For the WFE/BE analysis presented in this paper, a software program, called WANDS, is used [28, 29].

Consider a structure which is infinitely long in one direction, here denoted the x-direction, and has a uniform cross-section in the (y, z) plane which is discretised into finite elements. In WFE analysis, the partial differential equation of the structure is written in the form

$$\left[\mathbf{K_2}\frac{\partial^2}{\partial x^2} + \mathbf{K_1}\frac{\partial}{\partial x} + \mathbf{K_0} - \mathbf{M}\frac{\partial^2}{\partial t^2}\right]\mathbf{U}(x,t) = \mathbf{F}(x,t)\,, \tag{1}$$

where $\mathbf{K_2}$, $\mathbf{K_1}$ and $\mathbf{K_0}$ are stiffness matrices, $\mathbf{M}$ is the mass matrix of the cross-section, $\mathbf{U}(x,t)$ is the vector of displacements of FE node points on the cross-section and $\mathbf{F}$ is the corresponding external force vector. (If plate elements are employed, a fourth order differential term $\mathbf{K_4}\,\partial^4/\partial x^4$ is added in the left-hand side of Eq. (1)). Since the structure is considered invariant in the x direction, all the matrices are independent of x. Introducing harmonic motion with respect to time with frequency ω and with respect to the x coordinate with wavenumber k_x, the displacement vector can be denoted as $\mathbf{U}(x,t) = \tilde{\mathbf{U}}e^{\mathrm{i}(\omega t - k_x x)}$ (and similarly the force vector), and then Eq. (1) becomes

$$\left[\mathbf{K_2}(-\mathrm{i}k_x)^2 + \mathbf{K_1}(-\mathrm{i}k_x) + \mathbf{K_0} - \omega^2\mathbf{M}\right]\tilde{\mathbf{U}} = \tilde{\mathbf{F}}\,, \tag{2}$$

where $\tilde{\mathbf{U}}$ indicates the displacements of the nodes corresponding to the particular wavenumbers and $\tilde{\mathbf{F}}$ is the corresponding amplitude vector of the external forces. By solving for wave solutions in the x direction, the FE model in Eq. (2) becomes two-dimensional over the cross-section. In addition, these wave solutions allow different wave types to be readily identified.

When the exterior of the waveguide structure is connected to a fluid domain, WBEs are introduced on the periphery of the structure to model the external fluid and these are coupled with the WFEs. For a given frequency ω and axial wavenumber k_x, the governing equation for the external fluid is given by

$$\mathbf{H}(k_n)\tilde{\mathbf{\Psi}} - \mathbf{G}(k_n)\frac{\partial\tilde{\mathbf{\Psi}}}{\partial\mathbf{n}} = \mathbf{0} \ , \tag{3}$$

where $\mathbf{H}$ and $\mathbf{G}$ are matrices of acoustic Green's functions, $\tilde{\mathbf{\Psi}}$ and $\frac{\partial\tilde{\mathbf{\Psi}}}{\partial\mathbf{n}}$ are vectors of the velocity potential and the normal velocity at the nodes of the boundary elements, and $\mathbf{n}$ is the unit normal vector of the WBEs, pointing out of the acoustic domain. In exterior radiation problems, 'CHIEF' points are used to overcome the non-uniqueness problem associated with resonances of the corresponding interior problem [30].

The wavenumber k_n in Eq. (3) is defined as shown in Fig.1 by

$$k_n = \sqrt{k_a^2 - k_x^2} \ , \tag{4}$$

where $k_a = \omega/c_0$ is the acoustic wavenumber and c_0 is the acoustic wave speed. k_n is referred to here as the radiation wavenumber because a structural wave with axial wavenumber k_x can radiate sound into the far field if k_n is real-valued, i.e., $k_a \geq k_x$. If $k_a < k_x$, Eq. (3) results in an acoustic near-field solution which radiates no sound power. Also, since k_n corresponds to the wavenumber component within the cross-sectional (y,z) plane, the direction of the radiated sound can be identified from the relation between k_x, which corresponds to the x direction, and k_n which corresponds to the (y,z) plane. This will be discussed further in Sec. 4.3 in terms of the longitudinal directivity of the rail noise.

In the coupling between the WFEs and WBEs, the pressure from the external fluid is applied as an additional load to the structure. Then the coupled WFE equation is given by

$$\left[\mathbf{K_2}(-\mathrm{i}k_x)^2 + \mathbf{K_1}(-\mathrm{i}k_x) + \mathbf{K_0} - \omega^2\mathbf{M}\right]\tilde{\mathbf{U}} - \mathrm{i}\omega\rho_0\mathbf{C_1}\tilde{\mathbf{\Psi}} = \tilde{\mathbf{F}} \ , \tag{5}$$

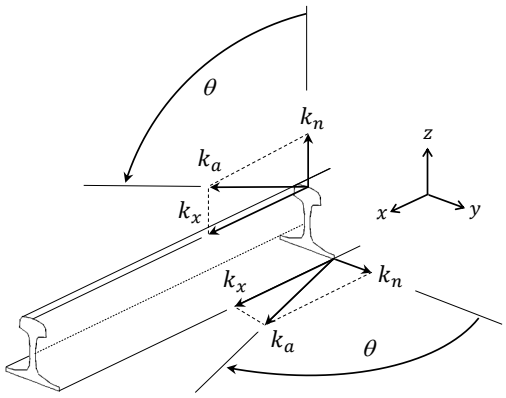

Figure 1: Radiation angle of the rail noise defined by a structural wavenumber k_x and radiation wavenumber k_n.

where $\mathbf{C}_1$ denotes a coupling matrix associating the coupled degrees of freedom (dofs) between the WFEs and WBEs and ρ_0 is the fluid density. The velocity continuity condition at the interface between the WFEs and WBEs is given by

$$\mathbf{I_2}\frac{\partial\tilde{\mathbf{\Psi}}}{\partial\mathbf{n}} = \mathrm{i}\omega\rho_0\mathbf{C_2}\tilde{\mathbf{U}} \ , \tag{6}$$

where $\mathbf{I_2}$ and $\mathbf{C_2}$ are matrices allocating coupled dofs in $\frac{\partial\tilde{\mathbf{\Psi}}}{\partial\mathbf{n}}$ and $\tilde{\mathbf{U}}$, respectively. For WBEs not coupled with WFEs, boundary conditions need to be specified. For each uncoupled WBE node, the boundary condition can be defined in the wavenumber domain by

$$C_a\,\tilde{p} + C_b\,\tilde{v}_n = C_c \ , \tag{7}$$

where $\tilde{p}$ denotes the sound pressure and $\tilde{v}_n$ is the fluid particle velocity in the normal direction [29]. For example, the locally reactive impedance (z_n) of WBE nodes can be specified with the coefficients C_a, C_b and C_c by

$$C_a = 1, \quad C_b = -z_n, \quad C_c = 0 \ . \tag{8}$$

Since the sound pressure $\tilde{p}$ and normal velocity $\tilde{v}_n$ can be obtained from the velocity potential by

$$\tilde{p} = \mathrm{i}\omega\rho_0\tilde{\Psi} \ , \quad \tilde{v}_n = -\frac{\partial\tilde{\Psi}}{\partial\mathbf{n}} \ , \tag{9}$$

Eq. (7) can be written in matrix form as

$$\mathrm{i}\omega\rho_0\mathbf{C_a}\tilde{\mathbf{\Psi}} - \mathbf{C_b}\frac{\partial\tilde{\mathbf{\Psi}}}{\partial\mathbf{n}} = \mathbf{C_c} \ . \tag{10}$$

Since a part of the boundary may couple to WFEs, the number of boundary conditions may be less than the number of nodes in the WBE model. Hence, $\mathbf{C_a}$, $\mathbf{C_b}$ and $\mathbf{C_c}$ in Eq. (10) may not be square matrices. The governing equation of the coupled WFE/BEs is given by

$$\begin{bmatrix} \mathbf{K}-\omega^2\mathbf{M} & -\mathrm{i}\omega\rho_0\mathbf{C_1} & \mathbf{0} \\ \mathbf{0} & \mathbf{H} & -\mathbf{G} \\ -\mathrm{i}\omega\rho_0\mathbf{C_2} & \mathbf{0} & \mathbf{I_2} \\ \mathbf{0} & \mathrm{i}\omega\rho_0\mathbf{C_a} & -\mathbf{C_b} \end{bmatrix} \begin{pmatrix} \tilde{\mathbf{U}} \\ \tilde{\mathbf{\Psi}} \\ \frac{\partial\tilde{\mathbf{\Psi}}}{\partial\mathbf{n}} \end{pmatrix} = \begin{pmatrix} \tilde{\mathbf{F}} \\ \mathbf{0} \\ \mathbf{0} \\ \mathbf{C_c} \end{pmatrix} \ , \tag{11}$$

where $\mathbf{K} = \mathbf{K_2}(-\mathrm{i}k_x)^2 + \mathbf{K_1}(-\mathrm{i}k_x) + \mathbf{K_0}$. By solving Eq. (11), the coupled structural and acoustic responses can be obtained.

The sound power radiated from the structure can be evaluated by integrating over the wavenumber domain:

$$W = \frac{1}{4\pi}\mathrm{Re}\left(\int_{-k_a}^{k_a}\int_{\Gamma}\tilde{p}^*(k_x)\tilde{v}_n(k_x)\mathrm{d}\Gamma\mathrm{d}k_x\right) \ , \tag{12}$$

where * denotes the complex conjugate and Γ is the perimeter of the cross-section in contact with fluid. Since sound can only be radiated from the structure when $k_x \le k_a$, as stated in Eq. (4), the integration with respect to k_x in Eq. (12) is limited to $-k_a \le k_x \le k_a$. The mean-squared velocity of the rail surface averaged over time and perimeter can be calculated by

$$\langle\overline{v^2}\rangle_{\mathrm{inf}} = \frac{1}{2\pi\Gamma}\int_{-\infty}^{\infty}\int_{\Gamma}\frac{|\tilde{v}_n(k_x)|^2}{2}\mathrm{d}\Gamma\mathrm{d}k_x \ , \tag{13}$$

Table 1: Properties for the track modelling.

Rail mass per unit length	60.3 kg/m	Young's modulus of railpad (vertical)	11.6 MPa
Young's modulus of rail	210 GPa	Young's modulus of railpad (lateral)	1.6 MPa
Poisson's ratio of rail	0.3	Damping loss factor of railpad	0.3
Damping loss factor of rail	0.02		

where the subscript $_{\text{inf}}$ indicates an integral over the infinite extent in the x direction rather than an average. Unlike the sound power in Eq. (12), the range of integration for k_x in Eq. (13) is unbounded. However, in the practical implementation of Eq. (13), the integration is limited to the range from $-k_{\text{max}}$ to k_{max}, where k_{max} needs to be chosen to be sufficiently greater than the highest wavenumber k_x of the propagating waves at the frequency ω under consideration. The radiation ratio can be determined from the sound power and integrated mean-squared velocity obtained from Eqs (12) and (13), as

$$\sigma = \frac{W}{\rho_0 c_0 \Gamma \langle \overline{v^2} \rangle_{\text{inf}}} \quad . \tag{14}$$

Since the governing equation in Eq. (11) possesses two variables ω and k_x, it is required to have a double loop calculation with respect to them to perform 3D analysis in this wavenumber domain approach. Due to this double loop calculation, computing times can be quite long, particularly if a large number of dofs are required for the model. Therefore, a simplified calculation avoiding the double loop would be more practical and efficient if it gives comparable results to the full 3D analysis. A simplified 3D analysis adopted in the present study will be discussed in Sec. 4.2.

3. Modelling the track and ground

In a typical railway track, the rail is mounted directly on the sleepers but between the sleepers there is a gap between the bottom of the rail and the ground (either ballast or concrete slab). In order to consider these situations, three different acoustical models are examined: a rail in free space, a rail attached to the ground and a rail located at a certain height above the ground [18].

3.1. Rail and railpad model

In the study, only the rail and railpad are considered by neglecting the sleepers and ballast in the dynamic track model. This assumption may have some effect at low frequencies but is reasonable above the cut-on frequency of bending waves. The cross-sectional FE model used for the rail and railpad is shown in Fig. 2. A standard UIC60 rail and a railpad were modelled with 23 and 9 solid elements (all eight-noded), respectively. The bottom of the railpad is fixed rigidly. The total number of dofs in the track model is 372.

Since the WFE method requires that a waveguide structure has a uniform cross-section along the axial direction, the railpads are considered as a continuous elastic foundation in this track vibration model. Although the railpad is

modelled as a continuously distributed support, the radiation from the bottom of the rail foot can be still considered in the acoustic modelling by connecting the WBEs to the bottom of the rail foot and neglecting the railpad in the acoustic model (see Fig. 3(a) in Sec. 3.2). The railpad, shaded in Fig. 2, has a height of 1 cm. The properties used to represent the rail and railpad are listed in Table 1. The railpad was modelled as a massless orthotropic material to allow the vertical and lateral stiffnesses to be chosen independently. The elastic moduli of the railpad in the model correspond to stiffnesses for a single pad of 110 MN/m in the vertical direction and 15 MN/m in the lateral and longitudinal directions for a sleeper spacing of 0.63 m. The railpad properties in Table 1 were selected based on the typical values measured from operational slab tracks for high speed trains in Korea.

The external loads are applied at the top centre of the rail head in the vertical or lateral direction, as illustrated in Fig. 2. Since the UIC60 rail has a symmetric cross-section with respect to the vertical (z) axis, the vertical force applied on the centreline of the rail will only excite the waves which have symmetric cross-sectional deformations, e.g., the vertical bending wave, symmetric longitudinal wave, rail foot flapping wave, etc. On the other hand, the lateral load applied on the rail head will generate only the antisymmetric waves, such as the lateral bending wave, torsional wave, web bending wave, etc. [31].

3.2. Acoustical models for a rail with a ground

For the calculation of sound radiation from the rail, WBEs are employed and coupled with the WFEs at the rail surface. As considered in ref. [18], the ground can be included either directly under the rail or with a certain gap between them.

Three acoustical conditions are considered here, as illustrated in Fig. 3. In Fig. 3, the boundary elements are represented with thick red lines, which correspond to Γ in Eqs (12) and (13), in each model. For the rail in free space (Fig. 3(a)), the WBEs enclose the whole perimeter of the rail cross-section. For the rail attached to the ground in Fig. 3(b), the WBEs enclose the outer surface of the combined rail, railpad and ground. In case of the rail above the ground, the WBEs for the rail and ground are detached, as shown in Fig. 3(c).

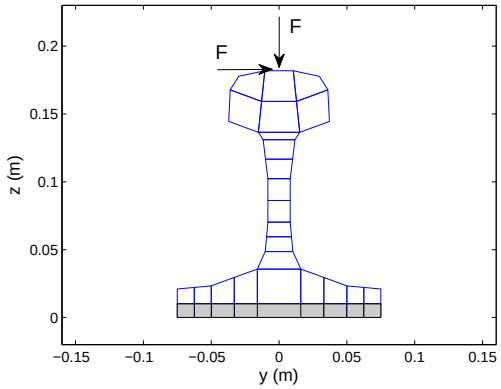

Figure 2: Cross-sectional model for the vibration of a rail and railpad. The shaded elements represent the railpad.

A direct BE method is implemented for the WBEs so the acoustic models for the rail and ground need to have closed shapes. The ground was therefore constructed as a large box for both the attached and detached grounds [18]. For simplicity, only the WBEs near the rail are displayed in Fig. 3(b) and 3(c). The ground model needs to be large enough to avoid disturbance from the edges [18]. The width of the ground model and the boundary element size were set differently for low and high frequency ranges. The box representing the ground is assigned a width of 10 m for frequencies below 400 Hz, 8 m for up to 1 kHz, 6 m for up to 2 kHz and 4m for up to 5 kHz. The size of the boundary elements for each case was set to 0.025 m, 0.02 m, 0.015 m and 0.01 m, respectively. According to these specifications, the widest half width of the ground box corresponds to the acoustic wavelength at 70 Hz and for the boundary element size of 0.01 m the ground model would be suitable for frequencies up to 5 kHz. The respective number of elements (all three-noded) used for the WBE models in Fig. 3 are 44, 442 and 446 and the corresponding numbers of WBE dofs are 208, 1808 and 1824, respectively.

In this acoustical modelling for the ground, a large number of WBEs is required. In the case of a rigid ground, however, the ground can be included more simply by introducing an image source for the rail and omitting the ground. In Sec. 5, these equivalent models will be used for predictions of rail noise with a rigid ground. A full 3D analysis can be performed for these equivalent models (as well as the rail in free space) due to their reduced number of WBE dofs.

For a ground with a finite impedance, however, the box-shaped ground model, having a large number of dofs, must be used. Hence, for the rail with impedance ground, a simplified 3D analysis is implemented by choosing a single dominant wave to avoid the double loop operation in the present study. That is, the calculation will be carried out only at a designated single wavenumber at each frequency. Details of this simplified 3D analysis will be discussed later in Sec. 4.2.

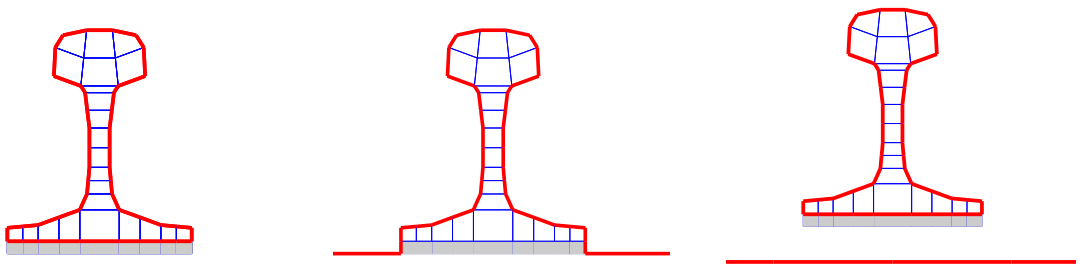

(a) (b) (c)

Figure 3: Boundary element models for a rail including the ground. (a) Rail in free space, (b) rail attached on ground, (c) rail above ground. The shaded parts represent the railpads which are not included in the WBE models for (a) and (c).

4. Rail noise in free space

Prior to including the ground in the model, the characteristics of the noise radiated from a rail in free space are investigated in this section.

4.1. Dispersion relation

Dispersion relations of propagating waves in the rail can be evaluated by solving for the free vibration from Eq. (2), setting $\tilde{\mathbf{F}} = \mathbf{0}$, and assuming that the acoustical WBE models presented in Fig. 3 have negligible effect on the structural response of the rail. Since the cross-section of the UIC60 rail is symmetric about the z axis, waves having symmetric and anti-symmetric cross-sectional deformations (vertical and lateral waves, respectively) are uncoupled and can be obtained separately [31].

Fig. 4(a) shows the dispersion curves of propagating waves having symmetric deformation modes with respect to the z axis. It is found from Fig. 4(a) that, for the rail investigated in this study, only two propagating waves occur below 5 kHz. These are, in the order in which they cut on, the longitudinal wave and the vertical bending wave. Another two waves (rail foot flapping and the second order longitudinal wave) occur above 5 kHz [7]. Fig. 4(b) shows the dispersion curves for the waves with anti-symmetric cross-sectional mode shapes with respect to the z axis. It can be seen from Fig. 4(b) that there are four waves with lateral motion propagating below 5 kHz. In the order that they cut on, they correspond to the lateral bending, torsional and the first and second order web bending waves [7]. Due to lower stiffness of the railpad in the lateral direction, the lateral bending wave has a lower cut-on frequency of 78 Hz, compared to 270 Hz for the vertical bending wave. The shapes of these vertical and lateral waves at $k_x = 0.1$ rad/m are illustrated in Figs 5 and 6 in the order that they cut-on. Since the two longitudinal waves in Fig. 4(a) possess

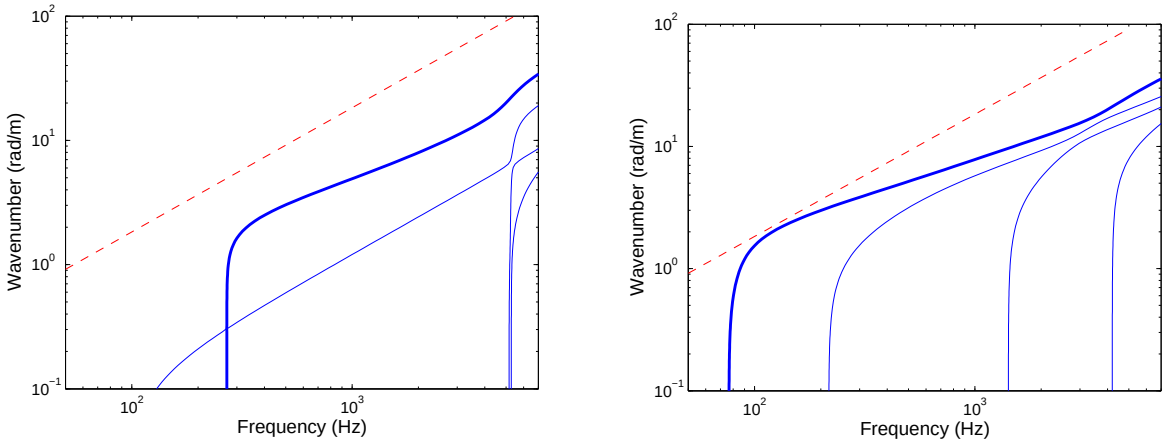

Figure 4: Dispersion diagrams of waves propagating along the rail. (a) Vertical waves, (b) lateral waves. Thick lines in each diagram represent the vertical and lateral bending waves, respectively. The acoustic wavenumber is also plotted with a dashed line.

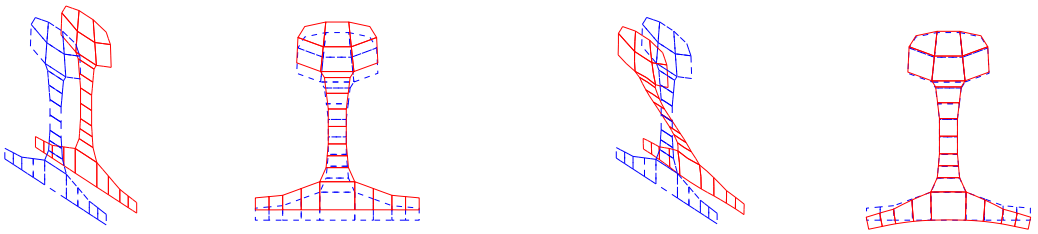

(a) (b) (c) (d)

Figure 5: Shapes of vertical waves in Fig. 4(a) at $k_x = 0.1$ rad./m. (a) Longitudinal wave at 130 Hz, (b) vertical bending wave at 270 Hz, (c) 2nd order longitudinal wave at 5157 Hz, (d) foot flapping wave at 5277 Hz. Dotted lines represent undeformed rail cross-section.

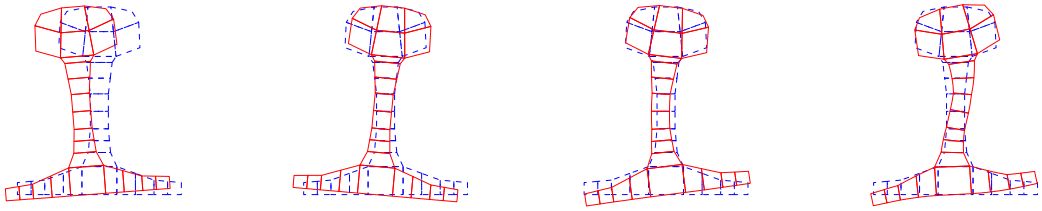

(a) (b) (c) (d)

Figure 6: Shapes of lateral waves in Fig. 4(b) at $k_x = 0.1$ rad./m. (a) Lateral bending wave at 78 Hz, (b) torsional wave at 217 Hz, (c) web bending wave at 1420 Hz, (d) 2nd order web bending wave at 4204 Hz. Dotted lines represent undeformed rail cross-section.

large deformation in the x-direction, they are plotted with a 3D view angle in Fig. 5 but the others are shown in the (y, z) plane. It should be noted that the wave shapes vary with frequency so that these descriptions of the waves do not necessarily apply at higher frequencies.

In Fig. 4, the vertical and lateral bending waves are distinguished by using thick lines because, as shown below, they are found to be the most important waves in each direction for the rail noise. For comparison, the acoustic wave is also plotted in the dispersion diagrams with a dashed line because only the waves below this line will radiate sound into the far field. Note that all the waves are well below the acoustic wavenumber apart from the lateral bending wave, which is very close to it around 130 Hz. The effect of this feature of the lateral bending wave will be discussed in terms of the rail noise later.

It is seen in Fig. 4 that veering of the curves associated with conversion of wave shapes takes place at high frequencies; around 5 kHz between the vertical waves and around 3 kHz among the lateral waves, respectively. Due to the wave conversion, for example, the waves from the top of the figure at 5 kHz in Fig. 4(b) correspond predominantly to web bending, lateral bending and torsional waves. Hence, precisely speaking, the waves chosen with the thick lines in Fig. 4 no longer correspond to the vertical or lateral bending wave after the wave conversion takes place. However, since the rail noise in this high frequency range is of less interest in this study, the waves presented with the thick lines

in Fig. 4 will be called the vertical and lateral bending waves for simplicity.

4.2. Sound radiation

In the rail model in free space shown in Fig. 3(a), all the WBEs are connected to the WFEs so that the additional boundary conditions described in Eq. (10) are unnecessary in forming the governing equation of Eq. (11). Furthermore, in the case of coupling with a light fluid, such as air, the fluid loading term containing $\mathbf{C}_1$ in Eq. (5) will have a negligible contribution to the structural response. Hence, the problem can be treated as a one-way coupling and then Eqs (2), (6) and (3) can be solved consecutively, instead of directly solving Eq. (11) with a matrix inversion [7]. That is, the structural response is solved first from Eq. (2) which is uncoupled with the fluid, and then the acoustic

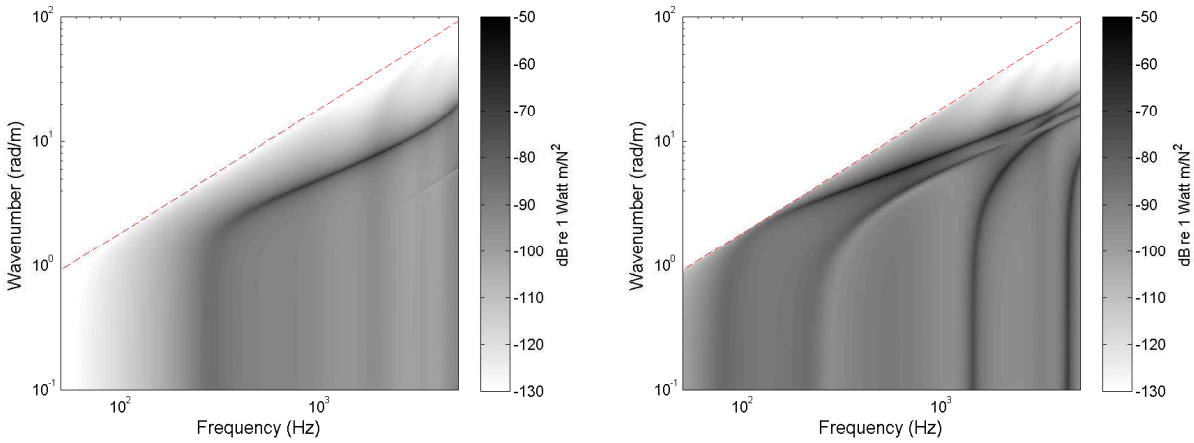

Figure 7: Image plot of the radiated power from the rail in free space for (a) vertical excitation, (b) lateral excitation.

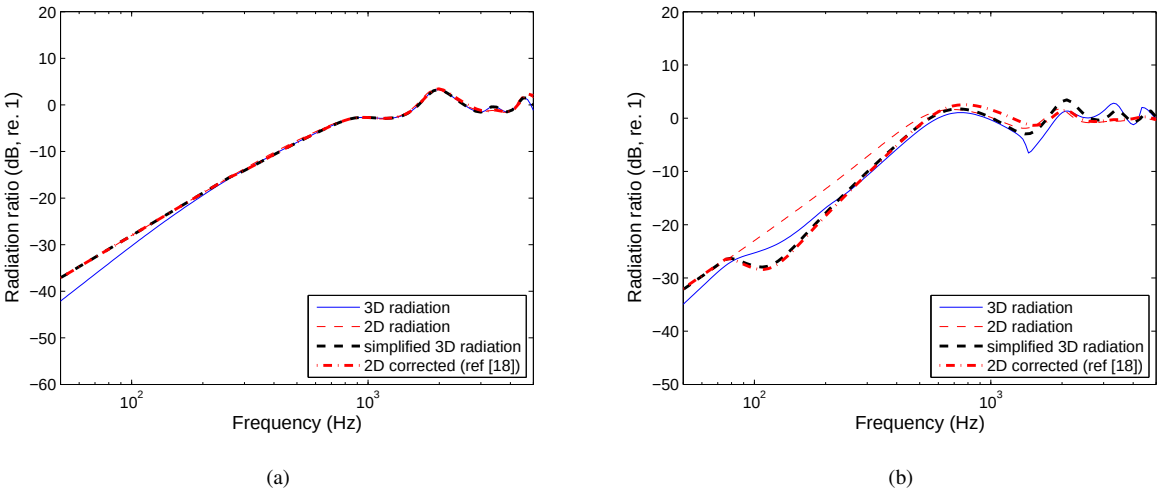

Figure 8: Radiation ratio of the rail in free space due to (a) vertical excitation, (b) lateral excitation.

responses $\partial\tilde{\boldsymbol{\Psi}}/\partial\mathbf{n}$ and $\tilde{\boldsymbol{\Psi}}$ are found by using Eq. (6) and Eq. (3), respectively. Note that a double loop operation over frequency and wavenumber is still required for the analysis even with this one-way coupling approach.

The sound power radiated from the rail in free space is presented in Fig. 7 in the form of image plots against frequency and wavenumber for a point force. For vertical excitation, comparison of Fig. 7(a) with Fig. 4(a) reveals that most of the rail noise is generated by the vertical bending wave. Although there is also a longitudinal wave in Fig. 4(a), it is not excited by the vertical force and consequently has negligible contribution to the sound radiation. For the lateral excitation, on the other hand, it can be seen from comparison of Fig. 7(b) and Fig. 4(b) that all four waves having lateral motion contribute to the sound radiation. Among them, however, the lateral bending wave is dominant from its cut-on frequency of 78 Hz, although the first web bending wave, which appears at 1420 Hz, also gives a considerable radiation above its cut-on frequency. It is confirmed from Fig. 7 that the rail noise between about 300 Hz and 2 kHz, where the rail is the main source of the rolling noise [5], comes mainly from the vertical and lateral bending waves.

These results can be expressed as a radiation ratio (Eq. (14)), as illustrated in Fig. 8 for the vertical and lateral excitations. Once the vertical and lateral bending waves cut on, at 270 Hz and 78 Hz respectively, the curve follows a trend of 30 dB/decade, consistent with the rail behaving as a line dipole source [7, 18]. Below these cut-on frequencies, where only rapidly-decaying evanescent waves exist near the excitation point, the rail behaves like a point dipole source, giving a trend of 40 dB/decade.

As frequency increases, the sound radiated from different parts of the rail cross-section interferes constructively and destructively leading to various humps and dips as seen in Fig. 8(a) and 8(b). This constructive and destructive interference can also be seen in Fig. 7 with darker and brighter vertical regions at high frequencies. Unlike the results for vertical bending, the radiation ratio in Fig. 8(b) falls below that of a line dipole (2D radiation in Fig. 8(b)) between

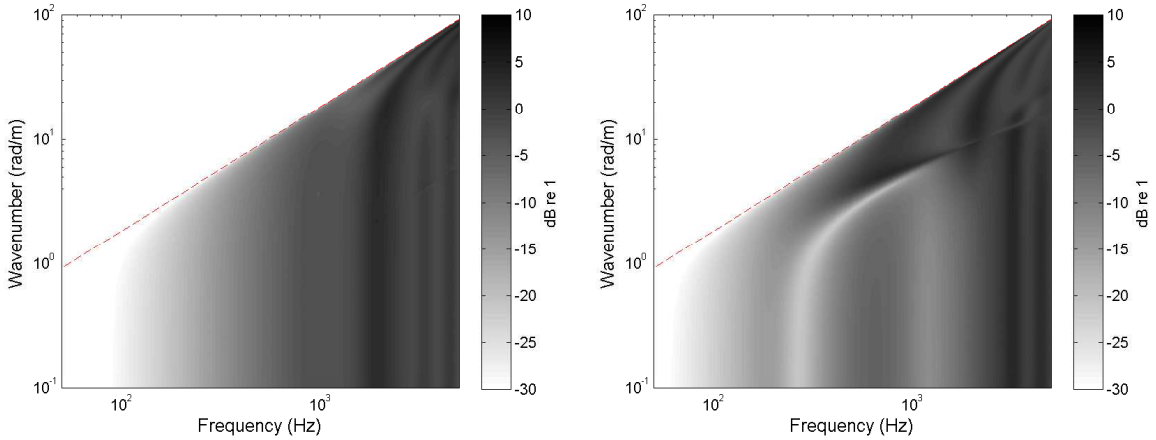

Figure 9: Image plot of the radiation ratio from the rail in free space for (a) vertical excitation, (b) lateral excitation.

about 80 Hz and 300 Hz. This is because the lateral bending wavenumber in this frequency region is very close to the acoustic wavenumber (Fig. 4(b)), implying that this wave does not behave like a line source in this frequency range [6, 18].

It is well reported in refs [6, 7, 18] that a two-dimensional (2D) approximation performs well in the prediction of the radiation ratio, apart from frequencies below the cut-on of the first bending wave. Since the rail behaves like a point dipole source in that low frequency region, the 2D assumption is no longer valid. Another limitation for the 2D assumption is that the structural wavenumber, k_x, should be small enough compared with the acoustic wavenumber, k_a, in order that the radiation wavenumber k_n in Eq.(4) is approximately equal to k_a. If k_x becomes similar to k_a, a correction is needed to the 2D model. This correction is necessary here for the lateral motion because the lateral bending wavenumber is quite close to the acoustic wavenumber around 130 Hz, as shown in Fig. 4(b). Zhang et al. [18] corrected their 2D BE model by using the radiation wavenumber of the bending waves in the 2D model, instead of using $k_x = 0$, and validated this with experiments.

The WFE/BE method performs a 3D analysis by carrying out a wavenumber domain calculation at each frequency. Hence, it will require much longer computing times than the 2D prediction, particularly for a model with a large number of dofs. Since the vertical and lateral bending waves were found to be most significant in the rail noise, a simplified 3D prediction is attempted based only on these single waves in each direction. That is, the WFE/BE calculation is performed for a single value of wavenumber at each frequency by tracing the dispersion curves of the bending waves (displayed with the thick lines in Fig. 4); for simplicity a 2D calculation with $k_x = 0$ is adopted below the corresponding cut-on frequencies. The computational benefit of the simplified 3D method depends on the number of wavenumber steps used in the full 3D analysis. In the present study, for example, 512 wavenumbers were used at each frequency to obtain the full 3D results. In terms of computational efficiency, therefore, the simplified 3D method will take 512 times less computing time than the full 3D analysis in the current model.

The radiation ratio predicted by the simplified 3D analysis is presented in Fig. 8 together with the full 3D results and the corrected 2D results proposed by Zhang et al. [18]. Note that the 2D correction is only applied for frequencies above the cut-on frequency of the vertical or lateral bending wave. It can be seen from Fig. 8(a), for the vertical motion, that the corrected 2D and simplified 3D results are nearly identical; they also give a good agreement with the full 3D results above the cut-on frequency of the vertical bending wave. On the other hand, for the lateral excitation, in Fig. 8(b), these two results coincide well with the full 3D radiation between 300 Hz and 1.5 kHz, while the simplified 3D result appears slightly better than the corrected 2D one at high frequencies. The simplified 3D model can be considered to be more realistic than the corrected 2D one because it involves the cross-sectional deformation while the corrected 2D model uses the undeformed rail cross-section. Unlike the vertical motion, however, there are considerable discrepancies between the full and simplified 3D results at around 120 Hz and 1.5 kHz for the lateral direction.

In order to see the radiation features of each wave more clearly, the radiation ratio is shown as an image plot against frequency and wavenumber in Fig. 9. The grey scale has a maximum value of 10 dB in Fig. 9; the maximum

values of the radiation ratio in Fig. 9(a) and 9(b) are both about 4 dB at around 2200 Hz and 17 rad/m. It can be observed from Fig. 9 that the vertical and lateral bending waves, which radiate most of the rail noise, are not clearly visible in these diagrams. This implies that these two bending waves are not particularly efficient in sound radiation but just possess large vibration levels leading to their dominant sound emission. From Fig. 9(b), it is found that the torsional wave is quite inefficient in the sound radiation. In addition, strong interferences are more clearly visible with vertical shaded regions in Fig. 9, e.g., a constructive interference around 2 kHz in Fig. 9(a) and around 3 kHz in Fig. 9(b).

To explain further the level differences seen in the radiation ratios predicted by the full and simplified 3D analyses for the lateral motion of the rail, the wavenumber spectra of the squared velocity, radiated power and radiation ratio are presented in Fig. 10 at four different frequencies, 120 Hz, 500 Hz, 1 kHz and 1.5 kHz. The results corresponding to the

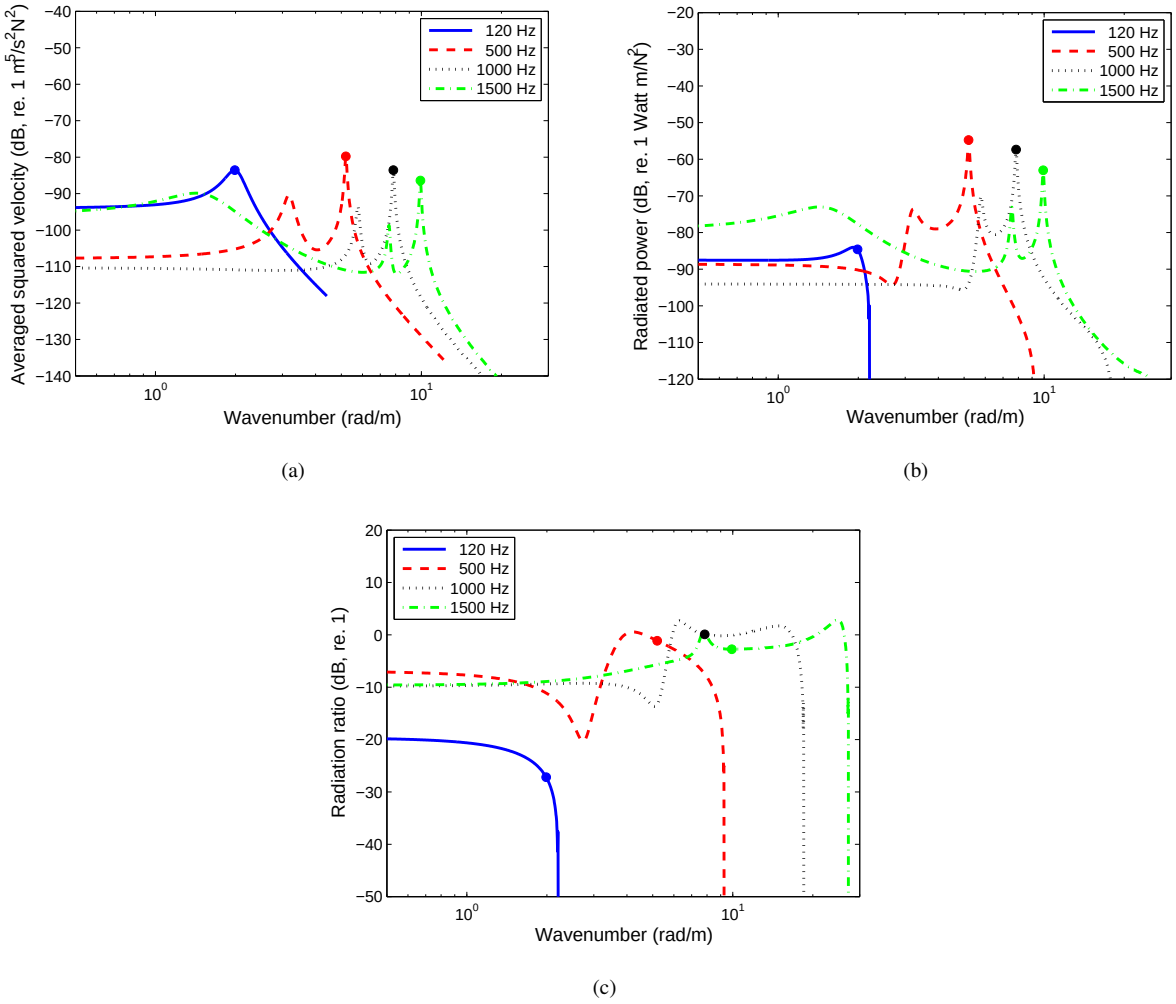

Figure 10: Wavenumber domain spectra for the rail in free space at four different frequencies for lateral excitation. (a) Averaged squared velocity, (b) radiated power, (c) radiation ratio.

lateral bending wavenumber at each frequency are marked with solid circles; these correspond to the values obtained from the simplified 3D calculation. Figs 10(a) and 10(b) show that the highest vibration and sound radiation are produced by the lateral bending wave at each frequency. However, the radiation ratios at these frequencies, presented in Fig. 10(c), clearly reveal that the highest radiation ratio is not from the lateral bending wave. Nevertheless, it is still close to the highest values and gives similar values to those of the full 3D analysis at 500 and 1000 Hz, as seen in Fig. 8(b). At 120 Hz, on the contrary, the radiation ratio of the lateral bending wave is much smaller than those at lower wavenumbers because the lateral bending wavenumber is very close to the acoustic wavenumber at this frequency; thus the simplified 3D method gives an underestimated value. Meanwhile, Fig. 10 shows that the overestimation of the simplified 3D result around 1.5 kHz in Fig. 8(b) is caused by the contribution of the web bending wave, which has a relatively low radiation ratio but is not included in the simplified 3D analysis.

4.3. Longitudinal directivity

The purpose in this section is to determine the direction of the sound radiation in the (x, y) plane for lateral motion or the (x, z) plane for vertical motion. Although not a conventional directivity, as the source is not compact, the results will be referred to here as the longitudinal directivity. The cross-sectional pressure distribution in the (y, z) plane of the rail in free space will be presented later in Sec. 6, together with those of rail models including the ground.

The radiated sound can be described by two wavenumbers, the axial wavenumber k_x and the wavenumber component in the (y, z) plane k_n. Hence the longitudinal direction of the rail noise can be identified in terms of an angle θ as illustrated in Fig. 1 by

$$\tan\theta = \frac{k_x}{k_n} = \left[\left(\frac{k_a}{k_x}\right)^2 - 1\right]^{-1/2} . \tag{15}$$

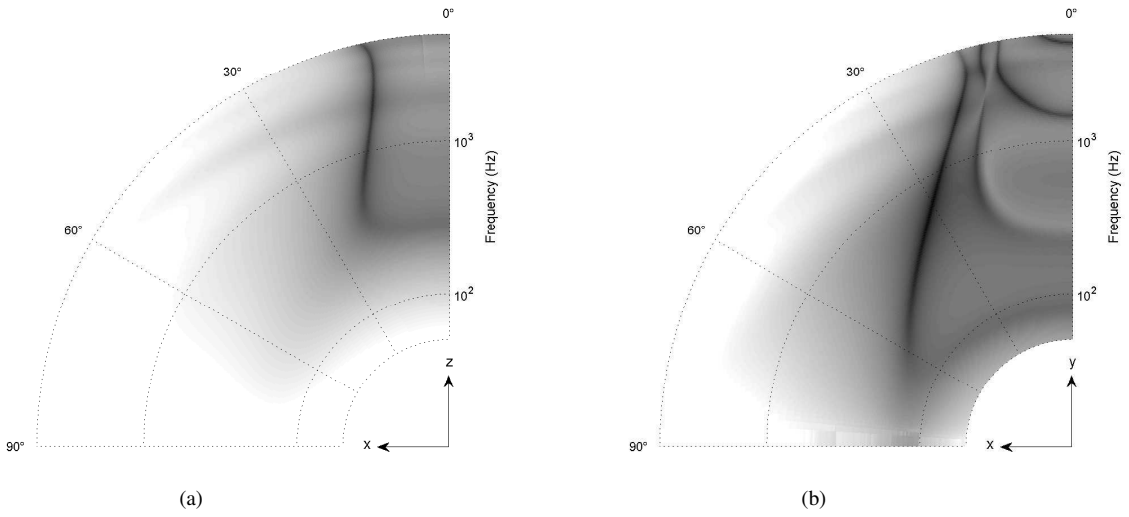

(a) (b)

Figure 11: Longitudinal directivity diagrams of the noise radiated from the rail in free space for (a) vertical excitation and (b) lateral excitation. The level of grey scale in these image plots is the same as those in Fig. 7.

Since the angle θ is a function of frequency and wavenumber, the image plot of the radiated power in Fig. 7 can be mapped into a directivity diagram in polar coordinates, as shown in Fig. 11. The wavenumber axis is converted to the angular axis and frequency is plotted in the radial direction. Then, $k_x = 0$ can be mapped onto $\theta = 0$ and the acoustic wavenumber k_a becomes $\theta = \pi/2$ (90°).

It can be seen from Fig. 11(a) that the vertical bending wave radiates sound in limited directions. At its cut-on frequency the radiation is in the direction of $\theta = 0°$, corresponding to a 2D radiation. The angle changes rapidly to about 20° at 300 Hz and then gradually decreases to 10° at 3 kHz, as described in refs [19, 20]. For the lateral motion, Fig. 11(b) shows that the lateral bending wave has a wider variation of the radiating direction as frequency increases. Starting at 0° at its cut-on frequency, it rapidly changes to about 70° at around 120 Hz due to the proximity of k_x to k_a (see Fig. 4(b)), before gradually decreasing to about 20° at 2 kHz. The sound radiated from the torsional and web bending waves is bounded to steeper angles less than 20°.

5. Rail noise with a rigid ground

In this section, the sound radiation from a rail with a rigid ground is investigated. In this analysis, the rigid ground is replaced with a mirrored imaginary rail and railpad to make the models simpler and smaller.

Two situations are considered, in which the rail is attached to the ground or located above the ground. The equivalent models are illustrated in Fig. 12. The boundary elements are plotted with thick red lines, which represent Γ in Eq. (12), and the shaded parts denote the railpad. The rail model detached from the ground is set to have a gap of 1 cm as its minimum and 5 cm as its maximum between the bottom of the rail foot and the ground (Fig. 12(b) is the model having a 5 cm gap). For these models, a full 3D calculation is performed using the one-way coupling condition.

The radiation ratios predicted from the equivalent models for vertical and lateral excitation are illustrated in

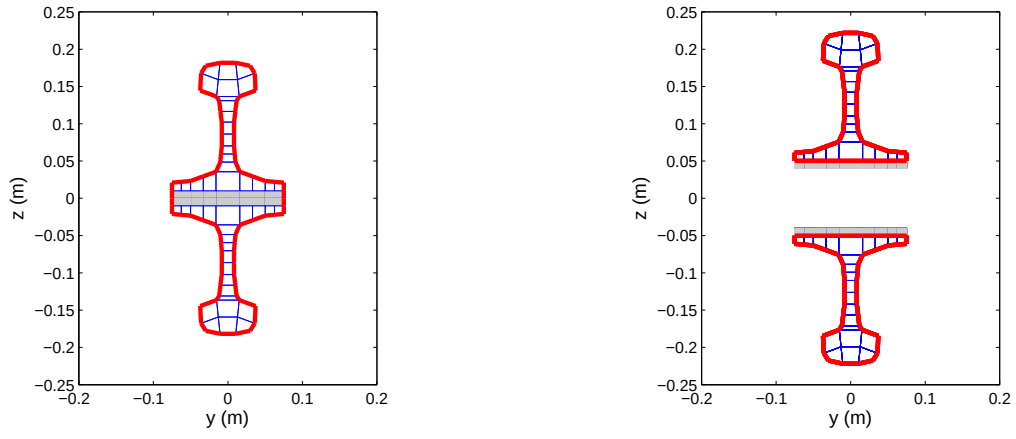

Figure 12: Equivalent WFE/BE models for a rail with a rigid ground. (a) Rail attached on rigid ground, (b) rail 5 cm above rigid ground.

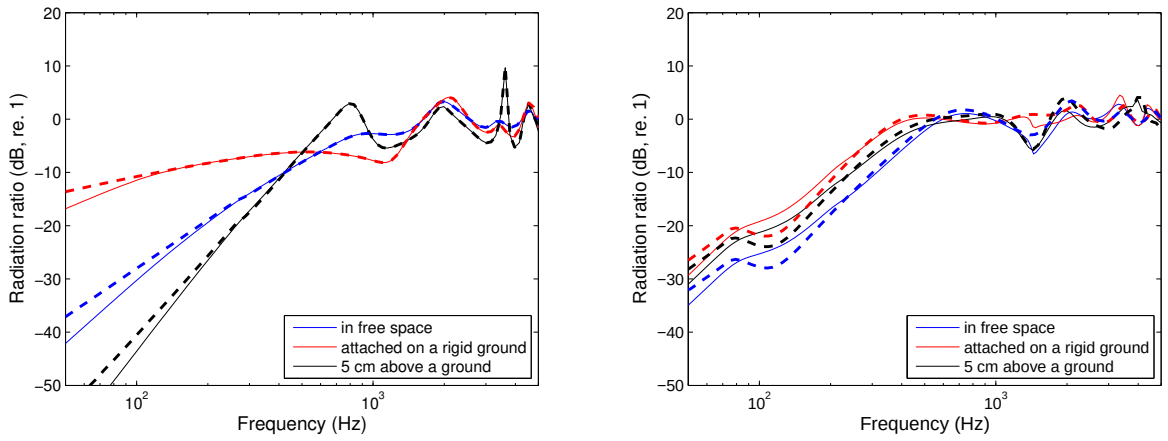

Figure 13: Comparison of the radiation ratio for the rail with and without a ground for (a) vertical motion and (b) lateral motion. Dashed lines are the simplified 3D results

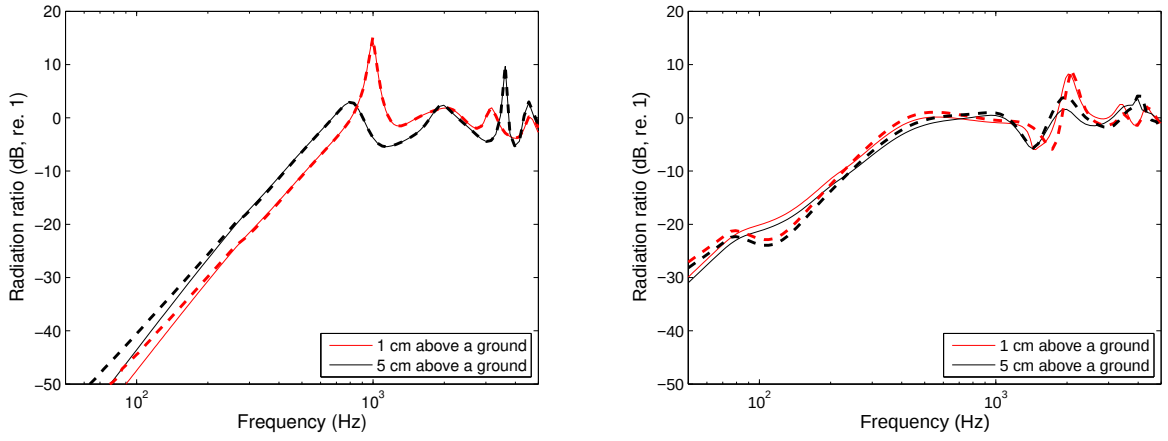

Figure 14: Comparison of the radiation ratio for the rail above the rigid ground in (a) the vertical motion and (b) the lateral motion. Dashed lines are the simplified 3D results.

Fig. 13, together with the results in free space. As shown by Zhang et al. [18], for the vertical motion in Fig. 13(a), the presence of the ground has a significant effect at low frequencies but little effect above about 1.5 kHz, except the strong resonance around 3.6 kHz occurring due to the 5 cm gap. Above the first cut-on frequency (270 Hz), the rail attached on the rigid ground behaves like a line monopole with a slope of 10 dB/decade whereas the rail above the ground behaves like a line quadrupole with a slope of 50 dB/decade [6, 7, 18]. This slope is greater in each case below the cut-on frequency. For the lateral motion, Fig. 13(b), the radiation ratio at low frequency has the same slope but a higher level in the presence of the ground; as shown by Zhang et al. [18] the real and image sources form two (point or

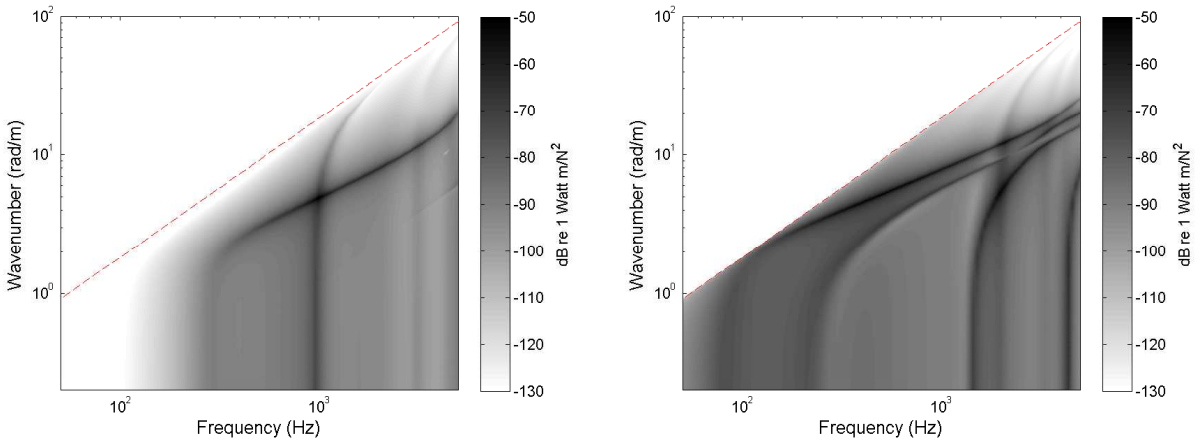

Figure 15: Image plot of the radiated power predicted from the rail 1 cm above a rigid ground for (a) vertical excitation and (b) lateral excitation.

line) dipoles moving in phase. At frequencies above 1 kHz, in each case there are dips and peaks due to interference, as described previously for the vertical motion.

The effect of the gap between the rail foot and the ground is shown in Fig. 14, which compares the results for gaps of 1 cm and 5 cm. A strong peak occurs at 1 kHz for a gap of 1 cm for the vertical motion. At this frequency the acoustic centres of the two opposing dipoles, formed by the rail and its image, are approximately half a wavelength apart leading to constructive interference [18]. As the gap grows, this peak reduces in amplitude but the rail noise from the vertical motion increases slightly at low frequency.

The simplified 3D results are also compared in Figs 13 and 14 with those from the full 3D analysis. It is found from this comparison that the simplified 3D prediction is still valid in the presence of a rigid ground at frequencies from at least 400 to 2000 Hz, where the rail is often the most significant source in rolling noise. Therefore, in further analysis for a rail with a ground represented by an impedance in Sec. 6, the simplified 3D prediction will be used, by taking a single bending wave for each direction. Note that, because there is no propagating wave below the cut-on frequency of the first bending wave, a 2D prediction will be used for these low frequencies for simplicity.

For the rail above the rigid ground with a gap of 1 cm, the radiated powers are presented as image plots in Fig. 15 for the vertical and lateral motions. It can be seen from Fig. 15(a) that the vertical bending wave is still the prominent sound radiator but makes less sound at low frequencies than that in free space (Fig. 7(a)). The strong constructive interference at 1 kHz seen in Fig. 14(a) is clearly displayed in Fig. 15(a) as a dark vertical shaded region. Other destructive interference is also visible as bright vertical regions at high frequencies. Fig. 15(b) confirms that the rail above a rigid ground radiates more sound from the lateral bending wave than that in free space (Fig. 7(b)). The destructive and constructive interferences are also observed around 1.3 kHz and 2 kHz with vertical shaded regions.

The radiated power diagrams can be replotted as longitudinal directivity diagrams but they look similar to those

for free space in Fig. 11, apart from the interference. For example, the constructive interference at about 1 kHz in Fig. 15(a) radiates wide directions from 0° to 60° varying rapidly with frequency. The directivity diagram is not presented here to avoid repetition.

6. Rail noise with a ground represented by an impedance

In this section, the effect of the ground impedance on rail noise is discussed in terms of the radiation ratio and the cross-sectional rail noise distribution. Since the vertical and lateral bending waves are the main radiators of the rail noise, the simplified 3D calculation is used here. That is, only a single wavenumber corresponding to the bending wave in each direction is chosen at each frequency in this simplified calculation thus avoiding the double-loop operation.

The surface impedance of the ground is represented by means of the Delany and Bazley model [32] with a specified flow resistivity. The locally reacting normal impedance is given in the Delany-Bazley model by

$$z_n = \rho_0 c_0 \left[1 + 9.08 \left(\frac{1000 f}{\sigma_e} \right)^{-0.75} - \mathrm{i}\, 11.9 \left(\frac{1000 f}{\sigma_e} \right)^{-0.73} \right] \tag{16}$$

where σ_e is the flow resistivity in units of Pa s/m^2. According to Eq. (16), values of lower flow resistivity correspond to a more absorptive ground (impedance closer to $\rho_0 c_0$). In this study various values of flow resistivity have been used, down to 5×10^4 Pa s/m^2, which is proposed for railway ballast in ref. [33]. (The rigid ground was modelled by using the mirrored image source as described in Sec. 5). The impedance evaluated by Eq. (16) is implemented as the boundary condition of WBEs for the ground at each frequency as described in Eq. (8).

This Delany and Bazley model in Eq. (16) may not be physically sophisticated for the acoustical characteristics of the ballast. However, for the purpose of examining the effect of the ground impedance on the noise radiated from the rail, this simple model allows the ground absorption to be varied using a single parameter σ_e.

6.1. Radiated sound

For both a rail attached on a ground and a rail placed 1 cm above it, the variation of the sound power due to the impedance of the ground is illustrated in Figs 16 and 17, respectively. Fig. 16(a) shows that, for vertical excitation, a rail attached on an impedance ground has its maximum radiation around 2 kHz regardless of the ground impedance and reduction of rail noise occurs mainly below about 1.2 kHz as the ground softens. For lateral excitation, Fig. 16(b) reveals that the highest rail noise occurs around 400 Hz (as seen in Fig. 7(b)), and rail noise from lateral motion is more affected by the absorptive ground in wider frequency range.

For a rail 1 cm above an impedance ground, Fig. 17(a) shows that the absorptive ground increases the rail noise at low frequencies, unlike the case for the rail attached on the ground. This seems to take place because the magnitude of the reflected sound from the ground is reduced and also its phase is changed as the ground becomes absorptive. Conversely, at high frequencies the rail above an impedance ground radiates less noise as the impedance reduces. Also, it can be seen that the peak at 1 kHz moves down to 550 Hz as the ground softens. For the lateral excitation,

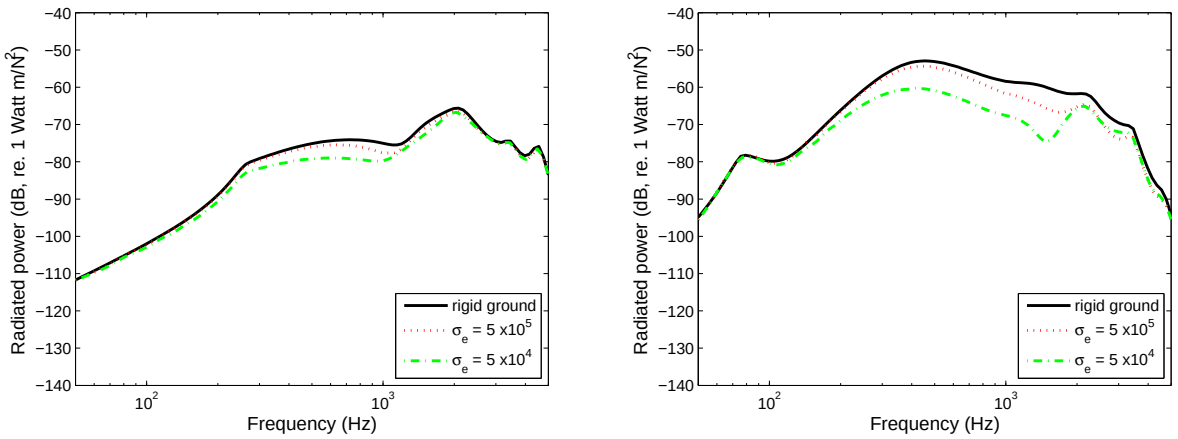

(a) (b)

Figure 16: Sound power radiated from the rail attached on the impedance ground for (a) vertical excitation and (b) the lateral excitation.

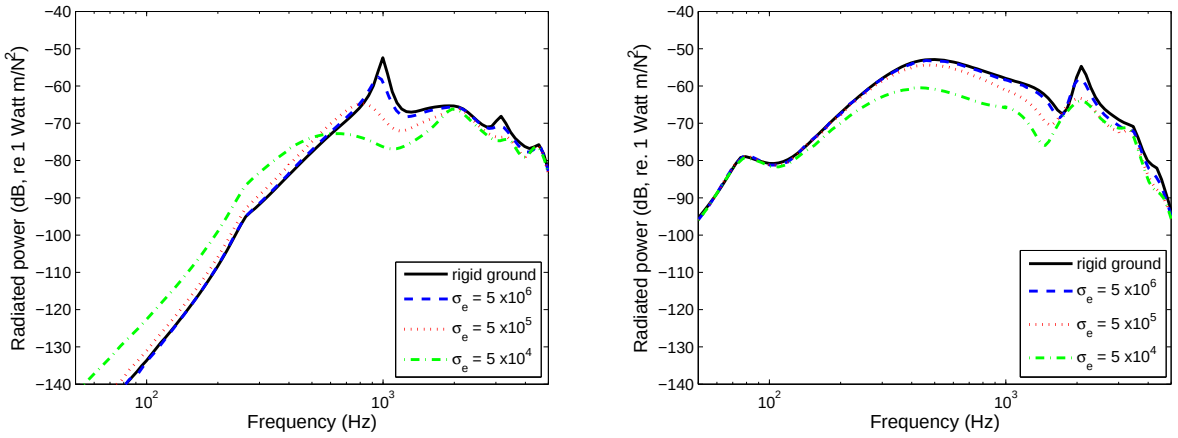

(a) (b)

Figure 17: Sound power radiated from the rail 1 cm above the impedance ground for (a) vertical excitation and (b) lateral excitation.

on the other hand, Fig 17(b) shows similar results to those in Fig 16(b); the rail radiates less sound as the impedance decreases.

In terms of the radiation ratio, the effect of the absorptive ground is illustrated in Figs 18 and 19, respectively. For a rail attached on a ground, Fig. 18 shows that a rail attached on an impedance ground radiates less sound around 1 kHz as the impedance decreases, particularly for the lateral motion, as explained in Fig. 16. As frequency increases, the ground impedance will be reduced and become closer to the impedance of air so that the radiation ratio becomes similar to that in free space at high frequencies (see Fig. 8).

The results for a rail above an impedance ground are shown in Figs 19 and 20 for 1 cm and 5 cm gaps between the rail and ground, respectively. For the vertical bending wave, it can be clearly seen from Fig. 19(a) that the strong

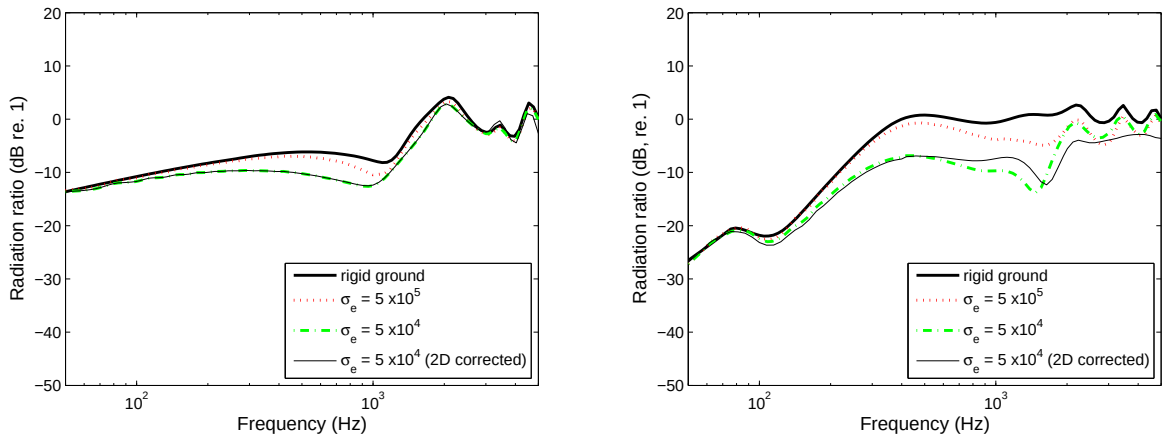

(a) (b)

Figure 18: Radiation ratio of the rail attached on the impedance ground for (a) vertical excitation and (b) the lateral excitation.

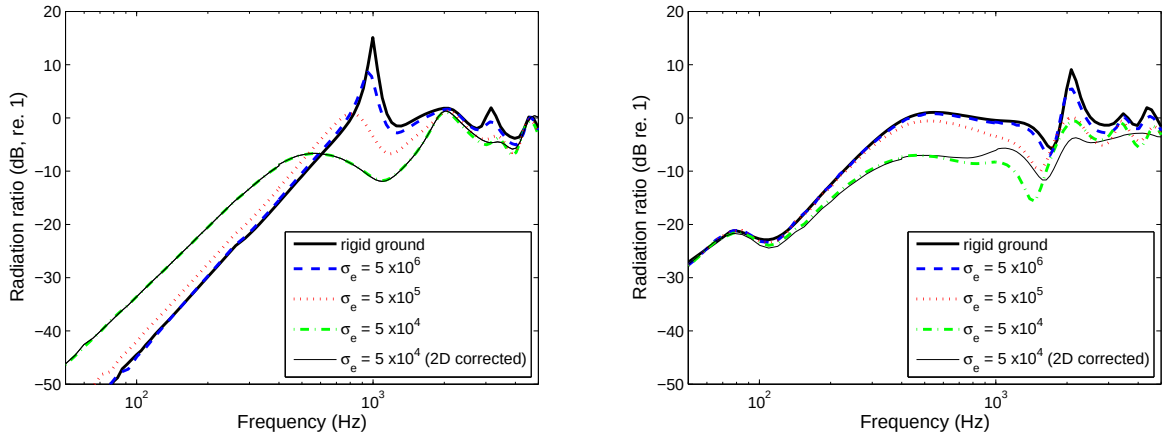

(a) (b)

Figure 19: Radiation ratio of the rail 1 cm above the impedance ground for (a) vertical excitation and (b) lateral excitation.

interference peak at 1 kHz due to the ground moves down in frequency as the ground becomes softer. For the increased gap of 5 cm, Fig. 20(a) shows that the effect of the ground impedance on the rail noise becomes less as the distance between the rail and the ground increases. For the lateral excitation, since the results in Figs 19(b) and 20(b) are fairly similar, this implies that the rail noise from lateral motion becomes less sensitive to the size of the gap within 1 to 5 cm range as the impedance decreases.

For comparison, the radiation ratios obtained from the 2D corrected model for $\sigma_e = 5 \times 10^4$ Pa s/m^2 are also presented in Figs 18, 19 and 20. It can be found from this comparison that the 2D corrected model coincides well with the simplified 3D model for vertical motion in the whole frequency range, regardless of the ground model. For lateral motion, however, although they show good agreement at low frequency the discrepancy between the two

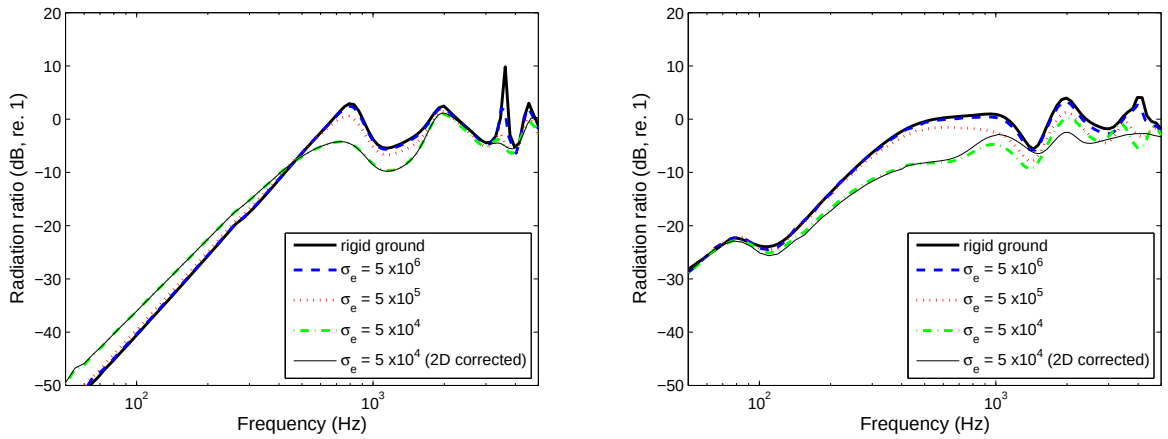

Figure 20: Radiation ratio of the rail 5 cm above the impedance ground for (a) vertical excitation and (b) lateral excitation.

approximate models grows as frequency increases. Since the 2D corrected model assumes that the vertical and lateral bending waves have an undeformed rail cross-section, the simplified 3D model is more appropriate for the prediction of radiation from the lateral motion of the rail.

6.2. Cross-sectional rail noise distribution

The cross-sectional sound pressure distribution of rail noise in the (y, z) plane is investigated in this section by means of the simplified 3D calculation for the vertical and lateral bending waves. In this prediction, three different frequencies, 500 Hz, 1 kHz and 1.5 kHz, are chosen to investigate the variation of the cross-sectional rail noise caused by the impedance of the ground. Longitudinal radiation angles of the rail noise at these frequencies can be obtained from Eq. (15) as 20°, 16° and 14° for the vertical bending wave and 34°, 26° and 22° for the lateral bending wave. Since the rail noise is calculated at a single wavenumber at each frequency, the cross-sectional pressure distribution (or directivity) will be independent of the x coordinate.

The field points used to obtain the cross-sectional pressure distribution are chosen with two different radii from the centre of the rail foot. They are 1.37 m for 500 Hz, which corresponds to twice the acoustic wavelength, and 0.7 m for both 1 kHz and 1.5 kHz, which is more than twice the acoustic wavelength. These field points are also more than an acoustic wavelength away from the edge of the ground plane to avoid interference from it. The vertical direction corresponds to 0° and 30 discrete angles are considered with a 3° interval up to 87°.

The distribution of sound pressure in the (y, z) plane, radiated from the vertical bending wave, is illustrated in Figs 21 and 22 for the rail attached on the ground and 5 cm above it, respectively, together with those for free space. Fig. 21(a) shows that the rail in free space has a vertical dipole radiation at 500 Hz but this changes to be more like a monopole when the rail is attached on the ground. It can be observed from Fig. 21(a) that the attached ground slightly reduces the rail noise around the vertical direction but considerably increases it around the lateral direction. At this

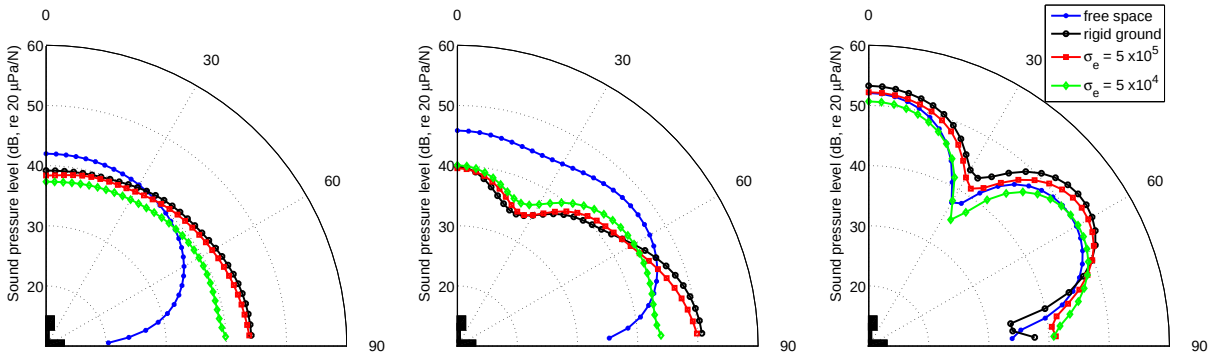

(a) (b) (c)

Figure 21: Cross-sectional rail noise radiated by the vertical bending wave for the rail attached on the impedance ground at (a) 500 Hz, (b) 1 kHz and (c) 1.5 kHz.

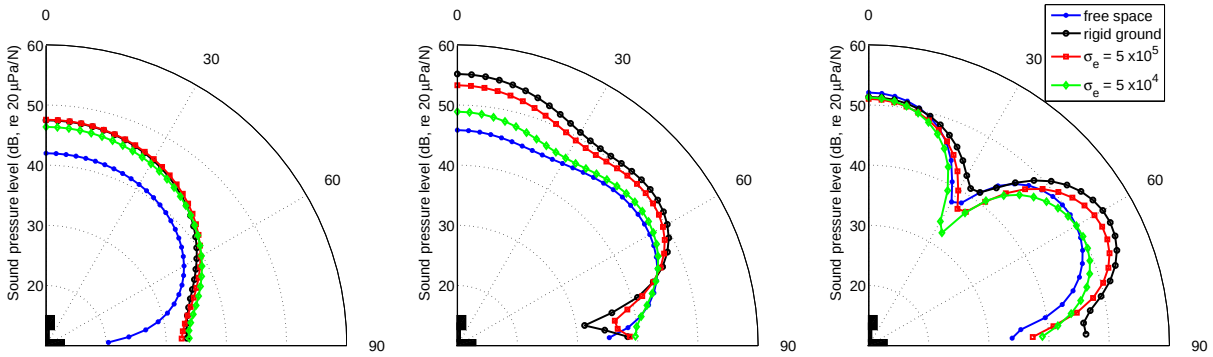

(a) (b) (c)

Figure 22: Cross-sectional rail noise radiated by the vertical bending wave for the rail 5 cm above the impedance ground at (a) 500 Hz, (b) 1 kHz and (c) 1.5 kHz.

frequency, softer ground reduces the rail noise in all directions, with a larger reduction horizontally. For the rail noise at 1 kHz, Fig. 21(b) shows that when the rail is attached on the ground, the rail radiates 5~10 dB less sound between 0° and about 70° while it gives increased emission close to the ground. Unlike the results in Fig. 21(a), softer ground tends to increase the rail noise slightly in directions less than about 60° but reduce it considerably in the close vicinity of the ground. It can be said from Figs 21(a) and 21(b) that the rail noise becomes less directional at 500 Hz and 1 kHz as the ground becomes softer. At 1.5 kHz, Fig. 21(c) shows that the rail gives strong radiation to about 0° and 55°; this radiating pattern appears less sensitive to the ground impedance and even to the presence of the ground. In terms of the sound level at 1.5 kHz, the attached rigid ground makes the rail noise increase in almost all directions except near the ground but as the ground becomes softer the rail noise tends to return to that of free space.

In the case of the rail 5 cm above the ground, Fig. 22(a) indicates that the rail becomes louder in all directions at

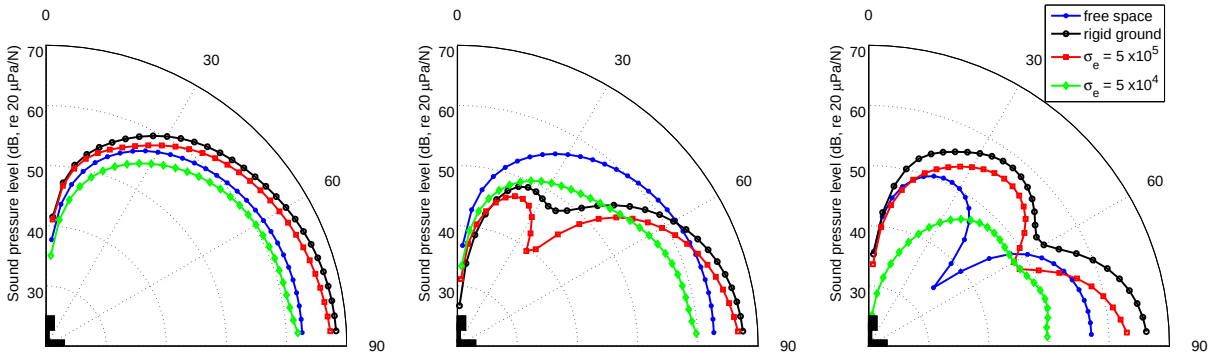

(a) (b) (c)

Figure 23: Cross-sectional rail noise radiated by the lateral bending wave for the rail attached on the impedance ground at (a) 500 Hz, (b) 1 kHz and (c) 1.5 kHz.

500 Hz in the presence of the ground, maintaining a dipole-like radiation. At 1 kHz, it is seen from Fig. 22(b) that the ground 5 cm below the rail amplifies the rail noise in upward directions up to about 70°. The rail noise, however, seems to approach back to that in free space as the ground becomes more absorptive. It can be seen from Fig. 22(a) and 22(b) that the rail has more radiation in the vertical direction at 500 Hz and 1 kHz due to the ground 5 cm below it. Fig. 22(c) at 1.5 kHz illustrates that the rail radiates most sound in the directions of 0° and 60° similarly to the case in Fig. 21(c), and more increment occurs around 60° due to the reflective ground. Also as the ground becomes softer, the rail noise at 5 cm above the ground seems close to that in free space. In terms of the directivity, it can be found from these results in Figs 21 and 22 for vertical excitation that the cross-sectional directivity pattern is not strongly affected by the impedance of the ground, apart from the case of the rail attached on the ground at 1 kHz shown in Fig. 21(b).

Cross-sectional rail noise predicted for the lateral bending wave is shown in Figs 23 and 24 for both ground models, together with those for free space. In each case the sound radiation is minimum in the vertical direction and the overall shape of the directivity is consistent with a horizontal dipole characteristic. The rail in free space behaves like a dipole source at 500 Hz and 1 kHz, while it has two directional lobes at about 25° and 90° at 1.5 kHz. For the rail attached to the ground, the sound pressure levels in Fig. 23(a) reveal that the rail still behaves like a lateral dipole source at 500 Hz even in the presence of the ground. Compared to the rail in free space, the rail on a reflective ground becomes noisier in all directions but the level reduces with more absorptive ground. Fig. 23(b) shows that the rail noise with two directional lobes at about 25° and 90° at 1 kHz is changed to a dipole radiation for $\sigma_e = 5 \times 10^4$ Pa s/m^2, making less noise than that in free space in all directions. At 1.5 kHz, Fig. 23(c) reveals that the rail noise increases with the rigid ground attached but the absorptive ground of $\sigma_e = 5 \times 10^4$ Pa s/m^2 reduces it considerably in vertical and lateral directions. According to Fig. 23, the attached rail gives similar directivity at all three frequencies for $\sigma_e = 5 \times 10^4$ Pa s/m^2.

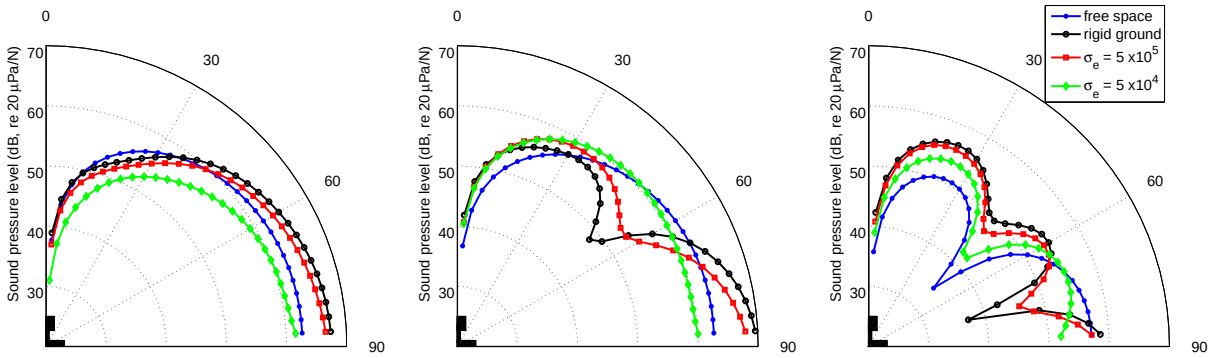

(a) (b) (c)

Figure 24: Cross-sectional rail noise radiated by the lateral bending wave for the rail 5 cm above the impedance ground at (a) 500 Hz, (b) 1 kHz and (c) 1.5 kHz.

In the case of the rail 5 cm above the ground, the sound pressure levels at 500 Hz in Fig. 24(a) represent similar features to those in Fig. 23(a). This implies that the 5 cm gap does not have a significant effect on the sound radiation for lateral motion at this frequency. On the other hand, the rail 5 cm above the ground shows slightly different directional patterns at 1 and 1.5 kHz, affected by the height of the gap. Fig. 23(b) shows that the rail noise at 1 kHz has a main lobe in the lateral direction for the rigid ground but this broadens considerably as the ground softens, making a strong reduction in the main lobe. Also, it is seen from Fig. 23(c) that a considerable change of directivity pattern occurs in directions greater than 60° at 1.5 kHz. Figs 24(b) and 24(c) show that the detached ground creates additional lobes but the directivity approaches that of the rail in free space as the ground impedance reduces. From the results in Figs 23 and 24 in terms of the directivity, the rail noise generated by the lateral bending wave seems to be affected more strongly by the impedance condition of the ground than for the vertical motion.

7. Conclusions

In this study, the noise radiated by a rail in the presence of a ground was investigated by means of the wavenumber domain finite and boundary elements method. The rail was considered radiating in free space, attached to the ground and located a certain distance above the ground.

From a full 3D calculation of the radiated power, it was observed that the vertical bending wave radiates most of the rail noise above its cut-on frequency up to about 5 kHz. For the lateral motion, on the other hand, four waves (the lateral bending, torsional and first and second web bending waves) contribute to the noise below 5 kHz, although the lateral bending wave is the dominant radiator in frequency range between about 80 Hz and 2 kHz. Hence, a simplified prediction was proposed using only these vertical and lateral bending waves for each direction, instead of performing a full 3D calculation at each frequency.

For the rail with the rigid ground, it was confirmed that the ground contributes quite differently to the rail noise

at low frequencies, depending on whether it is attached or detached acoustically to the rail. Introducing an absorptive ground, approximated with an impedance boundary condition, the rail noise is reduced in the whole frequency range in most situations. In the case of a rail vibrating vertically located above the ground, however, the rail noise grows at low frequencies as the ground impedance is reduced as the absorptive ground breaks the formation of a quadrupole source created by the rigid ground.

The directional distributions of rail noise in planes parallel and perpendicular to the rail were also investigated. In the plane parallel to the rail, the noise produced by the vertical motion has radiation angles limited between around 10° and 20° with respect to the axial direction while that from the lateral motion has a wider variation from about 15° to 70° depending on frequency. It was also observed that high noise levels caused by interference tend to have a wide range of radiation angles, varying rapidly with frequency.

The cross-sectional directivity patterns of the rail noise for the vertical motion were not strongly affected by the impedance of the ground although a considerable effect was seen at 1 kHz for the rail attached to the ground. For the lateral motion, the ground impedance had a stronger influence on the directivity at high frequencies.

Acknowledgement

This research was supported by the project “Development of railway noise and vibration reduction technology (17RTRP-B072484-05)” of the Ministry of Land, Infrastructure and Transport, Republic of Korea.

References

[1] P.J. Remington, Wheel/rail noise, part IV: rolling noise, Journal of Sound and Vibration 46 (1976) 419–436.

[2] P.J. Remington, Wheel/rail rolling noise, I: theoretical analysis, Journal of the Acoustical Society of America 81 (1987) 1805–1823.

[3] E.K. Bender and P.J. Remington, The influence of rails on train noise, Journal of Sound and Vibration 37 (1974) 321–334.

[4] D.J. Thompson, B. Hemsworth and N. Vincent, Experimental validation of the TWINS prediction program for rolling noise, part 1: description of the model and method, Journal of Sound and Vibration 193 (1996) 123–135.

[5] D.J. Thompson, P. Fodiman, H. Mahé, Experimental validation of the TWINS prediction program for rolling noise, part 2: results, Journal of Sound and Vibration 139 (1996) 137–147.

[6] D.J. Thompson, C.J.C. Jones and N. Turner, Investigation into the validity of two-dimensional models for sound radiation from waves in rails, Journal of the Acoustical Society of America 113 (2003) 1965–1974.

[7] C.-M. Nilsson, C.J.C. Jones, D.J. Thompson and J. Ryue, A waveguide finite element and bounary element approach to calculating the sound radiated by railway and tram rails, Journal of Sound and Vibration 321 (2009) 813–836.

[8] J. Ryue, D.J. Thompson, P.R. White and D.R. Thompson, Decay rates of propagating waves in railway tracks at high frequencies, Journal of Sound and Vibration 320 (2009) 955–976.

[9] J. Ryue, D.J. Thompson, P.R. White and D.R. Thompson, Wave reflection and transmission due to defects in infinite structural waveguides at high frequencies, Journal of Sound and Vibration 330 (2011) 1737–1753.

[10] L. Gavric, Computation of propagative waves in free rail using a finite element technique, Journal of Sound and Vibration 183 (1995) 531–543.

[11] L. Gry, Dynamic modelling of railway track based on wave propagation, Journal of Sound and Vibration 195 (1996) 477–505.

[12] I. Bartoli, A. Marzani, F. Lanza di Scalea, E. Viola, Modeling wave propagation in damped waveguides of arbitrary cross-section, Journal of Sound and Vibration 295 (2006) 685–707.

[13] W. Li, R.A. Dwight and T. Zhang, On the study of vibration of a supported railway rail using the semi-analytical finite element method, Journal of Sound and Vibration 345 (2015) 121–145.

[14] D. Hohenwarter, Railway noise propagation models, Journal of Sound and Vibration 141 (1990) 17–41.

[15] B. Plovsing and J. Kragh, Nord2000. Comprehensive outdoor sound propagation model. Part 1: Propagation in an atmosphere without significant refraction, DELTA Acoustics and Vibration Report, AV 1849/00, 2006.

[16] P. Jean, A variational approach for the study of outdoor sound propagation and application to railway noise, Journal of Sound and Vibration 212 (1998) 275–294.

[17] K. Attenborough, K.M. Li and K. Horoshenkov, Predicting outdoor sound, Taylor and Francis, 2007.

[18] X. Zhang, G. Squicciarini and D.J. Thompson, Sound radiation of a railway rail in close proximity to the ground, Journal of Sound and Vibration 362 (2016) 111–124.

[19] K. Kitagawa and D.J. Thompson, Comparison of wheel/rail noise radiation of japanese railways using the twins model and microphone array measurements, Journal of Sound and Vibration 293 (2006) 496–509.

[20] K. Kitagawa and D.J. Thompson, The horizontal directivity of noise radiated by a rail and implications for the use of microphone arrays, Journal of Sound and Vibration 329 (2010) 202–220.

[21] X. Zhang and H.G. Jonasson, Directivity of railway noise sources, Journal of Sound and Vibration 293 (2006) 995–1006.

[22] X. Sheng, C.J.C. Jones, D.J. Thompson, Modelling ground vibration from railways using wavenumber finite- and boundary-element methods, Proceedings of the Royal Society A 461 (2005) 2043–2070.

[23] C.-M. Nilsson, Waveguide finite elements applied on a car tyre, Ph. D. Thesis, KTH, Stockholm, 2004.

[24] C.-M. Nilsson and S. Finnveden, Waves in thin-walled fluid-filled ducts with arbitrary cross-sections, Journal of Sound and Vibration 310 (2008) 58–76.

[25] F. Birgersson, S. Finnveden and C.-M. Nilsson, A spectral super element for modelling of plate vibration. part 1: general theory, Journal of Sound and Vibration 287 (2005) 297–314.

[26] H. Kim, J. Ryue, Sound radiation from strip plates with longitudinal stiffeners using waveguide finite and boundary element methods, Journal of Mechanical Science and Technology 28 (2014) 2527–2534.

[27] H. Kim, J. Ryue, D.J. Thompson, and A.D. Müller, Prediction of radiation ratio and sound transmission of complex extruded panel using wavenumber domain finite element and boundary element methods, Journal of Physics: Conference Series 744 (2016) 012144.

[28] C. M. Nilsson, J. Ryue, and C. J. C. Jones, Manual for WANDS 2.2 Wavenumber domain software for solids and fluids, University of Southampton, 2010.

[29] C. M. Nilsson, J. Ryue, and C. J. C. Jones, Theory manual for WANDS 2.1 Wave-number-domain FE-BE software for structures and fluids, University of Southampton, 2010.

[30] H. Schenck, Improved integral formulation for acoustic radiation problem, Journal of the Acoustical Society of America 44 (1968) 41–58.

[31] J. Ryue, D.J. Thompson, P.R. White and D.R. Thompson, Investigation of propagating wave types in railway tracks at high frequencies, Journal of Sound and Vibration 315 (2008) 157–175.

[32] M.E. Delany and E.N. Bazley, Acoustical properties of fibrous absorbent materials, Applied Acoustics 3 (1970) 105–116.

[33] E.M. Salomons and D. Heimann, Description of the harmonoise reference model, Report HAR29TR-041118-TNO10, TNO, 2004.